Volume 11
Number 31
21 August 2020
Pages 8043–8326

Chemical Science

rsc.li/chemical-science

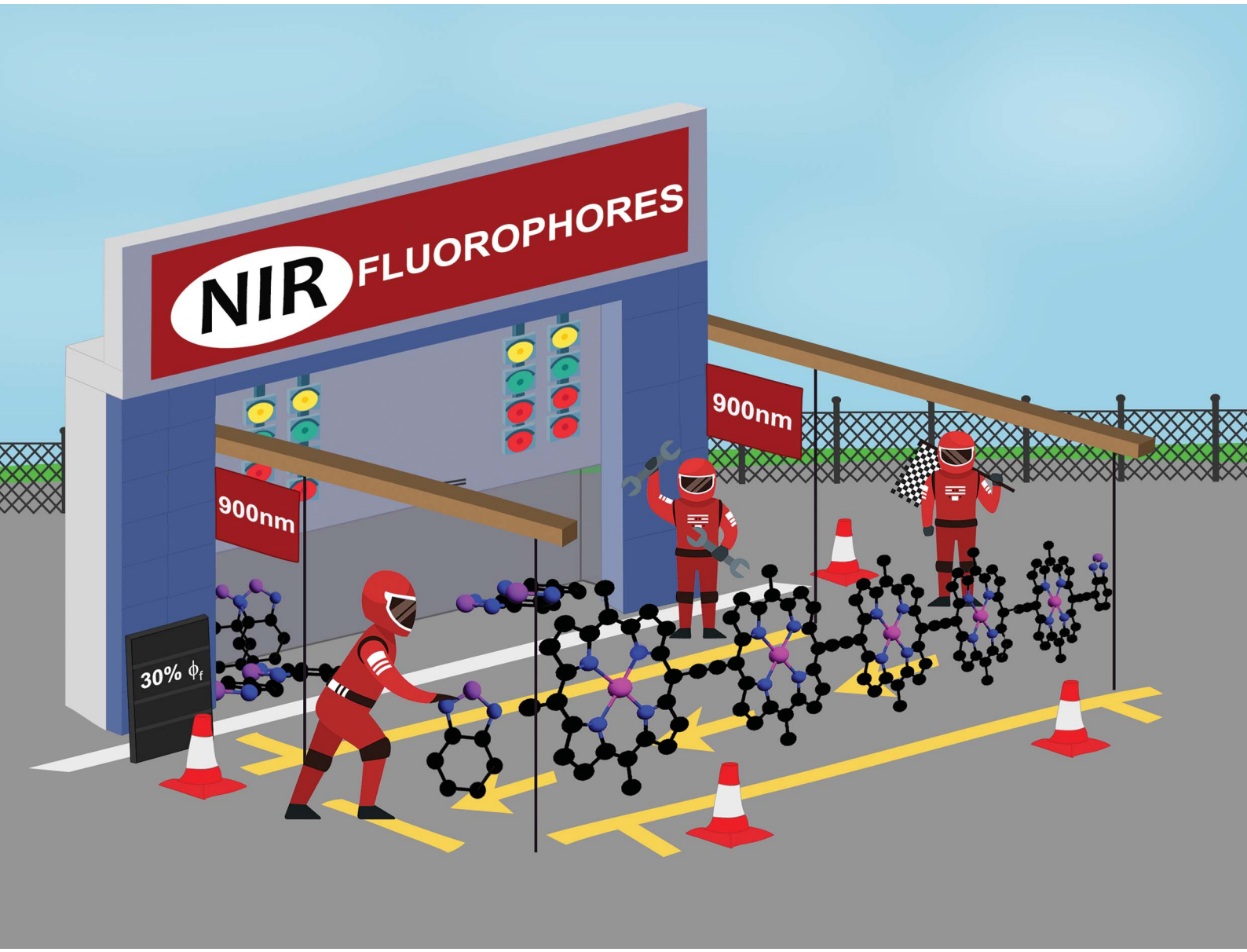

ISSN 2041-6539

ROYAL SOCIETY OF CHEMISTRY

EDGE ARTICLE

Michael J. Therien *et al.*

Driving high quantum yield NIR emission through proquinoidal linkage motifs in conjugated supermolecular arrays

Chemical Science

ROYAL SOCIETY OF CHEMISTRY

EDGE ARTICLE

View Article Online
View Journal | View Issue

Check for updates

Cite this: *Chem. Sci.*, 2020, **11**, 8095

All publication charges for this article have been paid for by the Royal Society of Chemistry

Open Access Article. Published on 05 Eost 2020. Downloaded on 2026-05-14 15:42:09.
This article is licensed under a Creative Commons Attribution-NonCommercial 3.0 Unported Licence.

Driving high quantum yield NIR emission through proquinoidal linkage motifs in conjugated supermolecular arrays†

Erin J. Peterson, Wei Qi, Ian N. Stanton, Peng Zhang and Michael J. Therien *

High quantum yield NIR fluorophores are rare. Factors that drive low emission quantum yields at long wavelength include the facts that radiative rate constants increase proportional to the cube of the emission energy, while nonradiative rate constants increase in an approximately exponentially with decreasing S_0–S_1 energy gaps (in accordance with the energy gap law). This work demonstrates how the proquinoidal BTD building blocks can be utilized to minimize the extent of excited-state structural relaxation relative to the ground-state conformation in highly conjugated porphyrin oligomers, and shows that 4-ethynylbenzo[*c*][1,2,5]thiadiazole (**E-BTD**) units that terminate *meso*-to-*meso* ethyne-bridged (porphinato)zinc (**PZn$_n$**) arrays, and 4,7-diethynylbenzo[*c*][1,2,5]thiadiazole (**E-BTD-E**) spacers that are integrated into the backbone of these compositions, elucidate new classes of impressive NIR fluorophores. We report the syntheses, electronic structural properties, and emissive characteristics of neoteric **PZn-(BTD-PZn)$_n$**, **PZn$_2$-(BTD-PZn$_2$)$_n$**, and **BTD-PZn$_n$-BTD** fluorophores. Absolute fluorescence quantum yield (ϕ_f) measurements, acquired using a calibrated integrating-sphere-based measurement system, demonstrate that these supermolecules display extraordinary ϕ_f values that range from 10–25% in THF solvent, and between 28–36% in toluene solvent over the 700–900 nm window of the NIR. These studies underscore how the regulation of proquinoidal conjugation motifs can be exploited to drive excited-state dynamical properties important for high quantum yield long-wavelength fluorescence emission.

Received 22nd June 2020
Accepted 14th July 2020

DOI: 10.1039/d0sc03446k

rsc.li/chemical-science

Introduction

Low band gap π-conjugated molecules and oligomers are central to function in electro-optic applications that span excitonic solar cells,[1–7] field-effect transistors,[8,9] optical power limiting (OPL),[10] dye-sensitized solar cells (DSSCs),[11,12] photon-upconversion (UC) technologies,[13–17] long-wavelength light-emitting diodes,[18–20] nonlinear optics (NLO),[21–24] and biological imaging.[25–27] Desirable low band gap materials for these applications typically feature singlet manifold transitions ($S_0 \rightarrow S_1$, $S_0 \rightarrow S_n$, and $S_1 \rightarrow S_n$) that possess large absorptive oscillator strengths covering broad spectral domains that include the near-infrared (NIR).

Driving high fluorescence quantum yields is perhaps the most demanding design challenge for low band gap chromophores. Engineering augmented $S_0 \rightarrow S_1$ transition oscillator strength is not sufficient to realize correspondingly high $S_1 \rightarrow S_0$ fluorescence quantum yields (ϕ_f values), particularly as the optical band gap is diminished: while it is often the case that a large $S_0 \rightarrow S_1$ absorptive extinction coefficient is correlated with a correspondingly large $S_1 \rightarrow S_0$ radiative rate constant congruent with the Strickler–Berg relationship,[28] most strongly

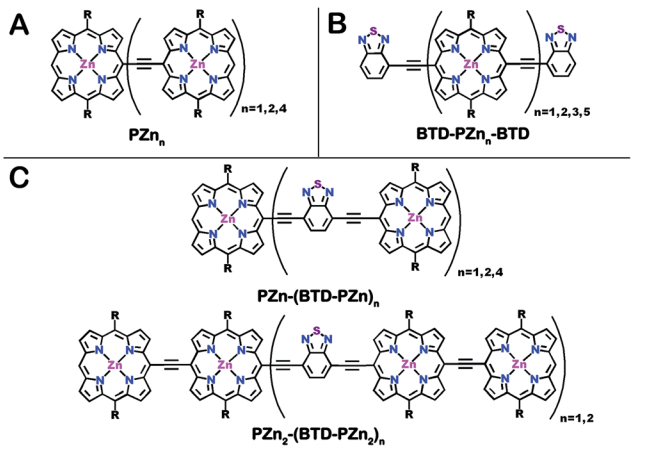

Chart 1 Chemical structures for (A) benchmark PZn$_n$, (B) BTD-PZn$_n$-BTD and (C) PZn$_2$-(BTD-PZn$_2$)$_n$ and PZn-(BTD-PZn)$_n$ fluorophores. R = [2,6-bis(3,3-dimethyl-1-butyloxy)phenyl].

Department of Chemistry, French Family Science Center, Duke University, 124 Science Drive, Durham, North Carolina 27708-0346, USA. E-mail: michael.therien@duke.edu

† Electronic supplementary information (ESI) available: Synthetic details, characterization data, additional spectroscopic and computational data. See DOI: 10.1039/d0sc03446k

Open Access Article. Published on 05 Eost 2020. Downloaded on 2026-05-14 15:42:09.
This article is licensed under a Creative Commons Attribution-NonCommercial 3.0 Unported Licence.

absorbing NIR chromophores are not impressive emitters, due to the substantial S_1 state non-radiative rate constants (k_{nr} values) that ensue from the energy gap law.[29]

With respect to high oscillator strength NIR absorbers, *meso*-to-*meso* ethyne-bridged (porphinato)zinc (**PZn$_n$**) arrays (Chart 1A)[17,30–46] constitute a notable exception to these generalizations. These supermolecules – conjugated structures realized from strong coupling of simple chromophoric building blocks – manifest such strong electronic and excitonic interactions between the constituent (porphinato)zinc oscillators that entirely unique photophysical entities are defined. **PZn$_n$** structures, for example, possess fluorescence quantum yields comparable to the most impressive NIR laser dyes in the 750–900 nm regime,[41] and rival the highest reported for organic dyes in this spectral window;[47–49] importantly, **PZn$_n$** emitters do not suffer from the commonly cited drawbacks of tricarbocyanine dyes that include poor photostability and fluorescence quantum yields that drop precipitously with decreasing solvent polarity.[25,50,51] **PZn$_n$** chromophores feature low energy Q-state derived π–π^* excited-states that are polarized exclusively along the long molecular axis, and lowest energy transitions that gain in intensity and progressively red-shift with increasing numbers of PZn units. Extended conjugation in these highly polarizable chromophores drives red-shifting of **PZn$_n$** fluorescence spectra. Because triplet excitons are more spatially confined than singlet excitons in these systems,[31,34,35,39,52,53] an unusual dependence of ϕ_f magnitude upon increasing emission wavelength [$\lambda_{max}(S_1 \rightarrow S_0)$] is manifest that confounds that anticipated simply from the energy gap law.[41] Because of this disparity in lowest energy singlet (S_1) and triplet (T_1) state delocalization, diminished S_1–T_1 intersystem crossing rate constants (k_{isc} values) track with increasing conjugation in **PZn$_n$** chromophores, and serve to partly counter-balance the impact of augmented Franck–Condon mediated internal conversion rate constants (k_{ic} values) that typically accompany diminished S_0–S_1 energy gaps in the NIR. These impressive **PZn$_n$** photophysical properties have been exploited in a wide range of fluorescence imaging applications.[54–61]

The photophysical properties of **PZn$_n$** chromophores may be extensively modulated *via* incorporation of proquinoidal units into these emblematic conjugated arrays. For example, proquinoidal spacer (Sp) moieties such as 4,7-diethynylbenzo[*c*][1,2,5]thiadiazole (**E-BTD-E**), 6,13-diethynylpentacene (**E-PC-E**), 4,9-diethynyl-6,7-dimethyl[1,2,5]thiadiazolo[3,4-*g*]quinoxaline (**E-TDQ-E**), and 4,8-diethynylbenzo[1,2-*c*:4,5-*c*′]bis([1,2,5]thiadiazole) (**E-BBTD-E**) that link bis[(porphinato)zinc] units can be utilized to modulate the relative degrees of quinoidal character that characterize the ground and electronically excited singlet states in these highly conjugated supermolecules.[62] Recent work highlights how electronic modulation of proquinoidal conjugation motifs can also be exploited as a powerful means to modulate independently the dynamics of excited-state relaxation pathways in these systems, enabling, for example, exceptional NIR absorbers that possess long-lived electronically excited triplet states (τ_{T1} > μs) that are generated at unit quantum yield.[63] In this contribution, we (i) show how proquinoidal BTD building blocks can be utilized to minimize the extent of excited-state structural relaxation relative to the ground-state conformation in highly conjugated porphyrin oligomers, and (ii) demonstrate that 4-ethynylbenzo[*c*][1,2,5]thiadiazole (**E-BTD**) units that terminate **PZn$_n$** chromophores (Chart 1B), and **E-BTD-E** spacers that are integrated into the backbone of these compositions (Chart 1C), enable elucidation of new classes of impressive NIR fluorophores.

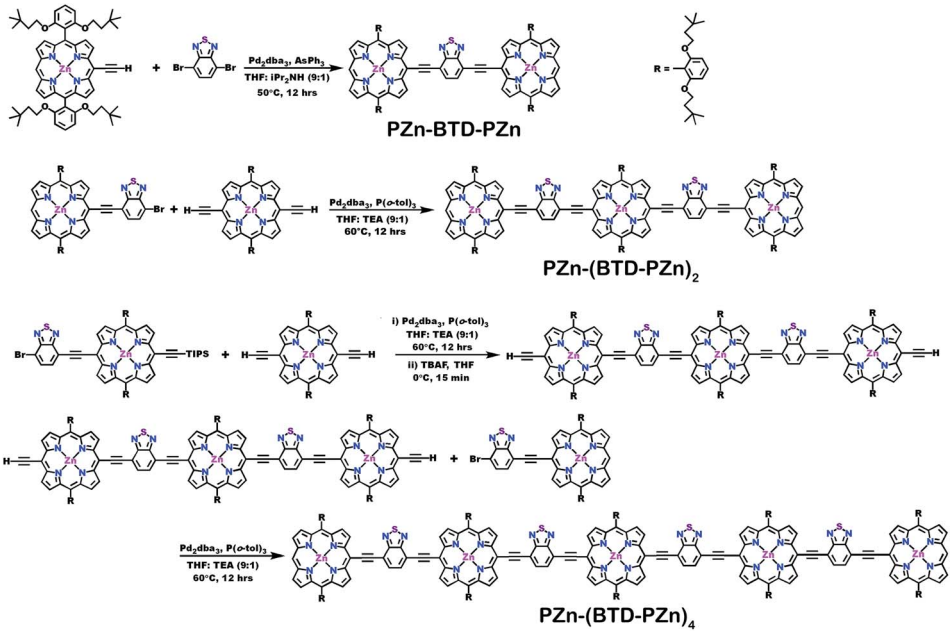

Scheme 1 Synthetic routes for PZn-(BTD-PZn)$_n$ compounds.

 This journal is © The Royal Society of Chemistry 2020

Open Access Article. Published on 05 Eost 2020. Downloaded on 2026-05-14 15:42:09.
This article is licensed under a Creative Commons Attribution-NonCommercial 3.0 Unported Licence.

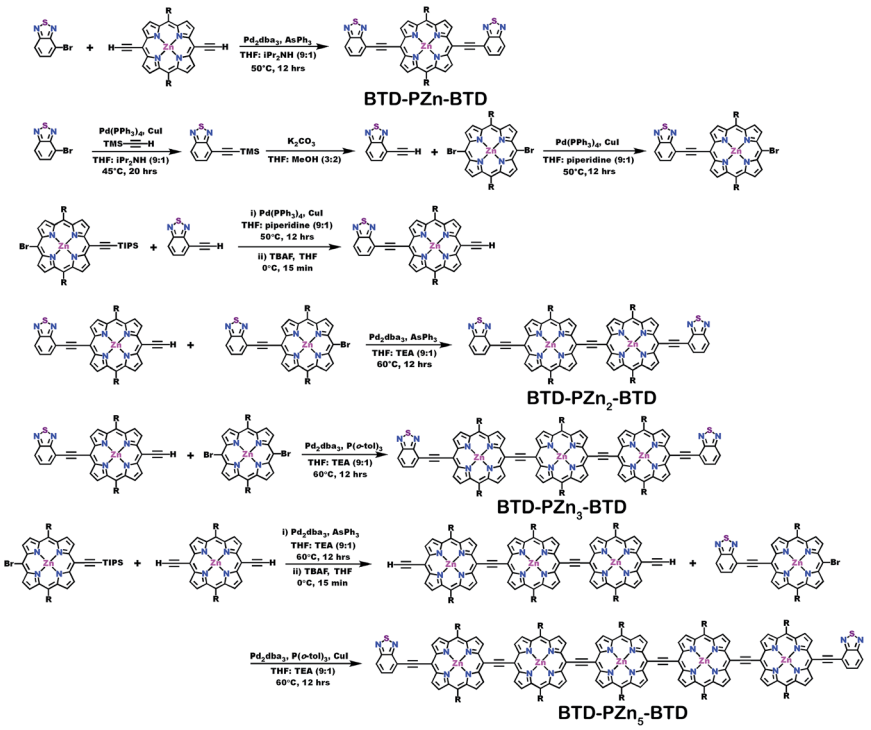

Scheme 2 Synthetic routes for BTD-PZn$_n$-BTD compounds.

Results and discussion

Synthesis

Schemes 1–3 outline the synthetic strategies for the fabrication of **BTD-PZn$_n$-BTD**, **PZn-(BTD-PZn)$_n$**, and **PZn$_2$-(BTD-PZn$_2$)$_n$** chromophores. These structures were synthesized by palladium (Pd)-mediated cross-coupling reactions involving appropriately substituted (porphinato)zinc(II) (PZn) compounds, BTD spacers, and terminal BTD units. These structures exploit [2,6-bis(3,3-dimethyl-1-butyloxy)phenyl] groups as 10- and 20-*meso*-porphyrin substituents, which facilitate solubility and straightforward assignment of ^{1}H-NMR spectra.[37,64] The nature of the functionalized **PZn**, **PZn$_n$**, and **BTD** moieties used in the syntheses of these **BTD-PZn$_n$-BTD**, **PZn-(BTD-PZn)$_n$**, and **PZn$_2$-(BTD-PZn$_2$)$_n$** arrays varied with the degree of conjugation in the precursor molecules. Synthetic details may be found in the ESI.†

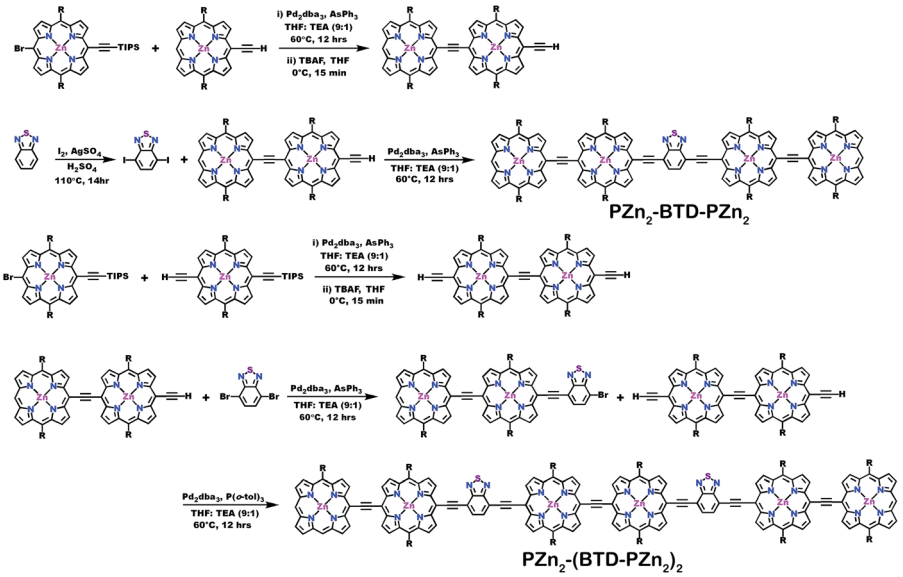

Scheme 3 Synthetic routes for PZn$_2$-(BTD-PZn$_2$)$_n$ compounds.

Open Access Article. Published on 05 Eost 2020. Downloaded on 2026-05-14 15:42:09.
This article is licensed under a Creative Commons Attribution-NonCommercial 3.0 Unported Licence.

Steady-state absorption and emission spectroscopy of BTD-PZn$_n$-BTD, PZn-(BTD-PZn)$_n$, and PZn$_2$-(BTD-PZn$_2$)$_n$ chromophores

Steady-state electronic absorption and fluorescence spectra recorded for reference **PZn$_n$** chromophores (**PZn$_2$**, **PZn$_3$**, and **PZn$_5$**; Fig. 1A),[17,30–46,54–56,58,59,61,63,65] as well as **PZn-(BTD-PZn)$_n$** [**PZn-BTD-PZn**,[62] **PZn-(BTD-PZn)$_2$**, and **PZn-(BTD-PZn)$_4$**; Fig. 1B], **PZn$_2$-(BTD-PZn$_2$)$_n$** [**PZn$_2$-BTD-PZn$_2$** and **PZn$_2$-(BTD-PZn$_2$)$_2$**; Fig. 1C], and **BTD-PZn$_n$-BTD** [**BTD-PZn-BTD**,[66] **BTD-PZn$_2$-BTD**, **BTD-PZn$_3$-BTD**, and **BTD-PZn$_5$-BTD**; Fig. 1D] arrays, are shown in Fig. 1. The overall characteristics of the electronic absorption spectra for these **PZn-(BTD-PZn)$_n$**, **PZn$_2$-(BTD-PZn$_2$)$_n$**, and **BTD-PZn$_n$-BTD** chromophores resemble those described previously for dimeric and multimeric PZn compounds that feature a *meso*-to-*meso* ethyne-linkage topology (**PZn$_n$** arrays); these spectra exhibit two distinct intense absorption manifolds that are derived from the porphyrin B- (Soret, $S_0 \rightarrow S_2$) and Q-band ($S_0 \rightarrow S_1$) transitions.[30,32–34,37,38,40]

The observed perturbations from these benchmark **PZn$_n$** spectra trace their origin to the proquinoidal BTD units that are connected to the porphyrin macrocycle *meso* carbons *via* ethynyl moieties. Previous investigations demonstrate that the nature of proquinoidal unit conjugation to the PZn macrocycle exerts a pronounced impact on the magnitude of B- and Q-state mixing;[62,63,66] for example, for PZn–(proquinoidal Sp)–PZn chromophores, the long axis-polarized Q state (Q_x) absorption maxima can be modulated from 689 to 1006 nm, depending upon the extent of the quinoidal resonance contribution to the electronically excited singlet state.[62] A combination of semi-empirical electronic structure calculations and electrochemical data underscore the cardinal role that PZn and proquinoidal fragment orbital energy differences play in fixing the radical cation and anion state energy levels in these structures.[62,63]

The principles that informed design of these **PZn-(BTD-PZn)$_n$**, **PZn$_2$-(BTD-PZn$_2$)$_n$**, and **BTD-PZn$_n$-BTD** chromophores stem from prior work that examined the photophysics of (porphinato)metal–(proquinoidal Sp)–(porphinato)metal supermolecules.[63] This work highlighted the central importance of the magnitude of the energy separation between the (porphinato)metal and proquinoidal Sp fragment frontier orbitals in determining whether radiative, internal conversion, or intersystem crossing decay channels dominated the relaxation dynamics of the initially prepared electronically excited states of these complexes. When the (porphinato)metal and proquinoidal Sp fragment LUMO levels featured energy separations on the order of a few tenths of an eV, as they are for the 5-ethynyl-PZn, 4-ethynyl-BTD, and 4,7-diethynyl-BTD fragments of these **PZn-(BTD-PZn)$_n$**, **PZn$_2$-(BTD-PZn$_2$)$_n$**, and **BTD-PZn$_n$-BTD** structures, chromophores having multiconfigurational S_1 states characterized by a modest degree of charge transfer (CT) character are anticipated; such supermolecules were shown to display large $S_1 \rightarrow S_0$ radiative rate constants and substantial fluorescence quantum yields. Other factors that informed the blueprint of the Fig. 1B–D supermolecules included insights derived from monomeric PZn complexes in which ethynyl-BTD units were used to expand conjugation at the macrocycle *meso*-carbon position;[66] these designs led to PZn chromophores characterized by enhanced transfer of B-to-x-polarized Q-state oscillator strength, intensified Q_x absorption bands, chromophore structural rigidification, spectrally narrow fluorescence emission bands, small magnitude Stokes shifts, and enhanced radiative rate constant magnitudes relative to simple benchmark PZn complexes.

Fluorescence emission metrics of BTD-PZn$_n$-BTD, PZn-(BTD-PZn)$_n$, and PZn$_2$-(BTD-PZn$_2$)$_n$ chromophores

Long wavelength absorption maxima (λ_{max}, $S_0 \rightarrow S_1$), corresponding extinction coefficient measurements, fluorescence ($S_1 \rightarrow S_0$) emission maxima, full-width at fluorescence half-

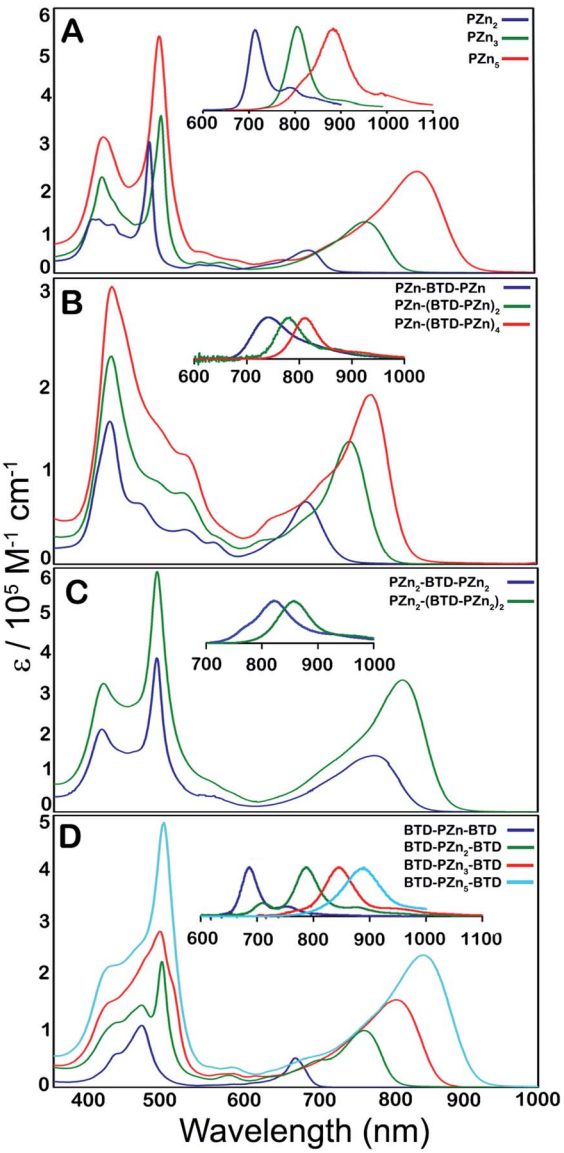

Fig. 1 Electronic absorption and emission spectra (figure panel insets) recorded for: (A) benchmark **PZn$_n$** chromophores (see ref. 30 and 41), and (B) **PZn-(BTD-PZn)$_n$**, (C) **PZn$_2$-(BTD-PZn$_2$)$_n$**, and (D) **BTD-PZn$_n$-BTD** compositions. Experimental conditions: T = 298 K, THF solvent.

This journal is © The Royal Society of Chemistry 2020

Open Access Article. Published on 05 Eost 2020. Downloaded on 2026-05-14 15:42:09.
This article is licensed under a Creative Commons Attribution-NonCommercial 3.0 Unported Licence.

Table 1 Electronic absorption and emission data in THF solvent for BTD-PZn$_n$-BTD, PZn-(BTD-PZn)$_n$, and PZn$_2$-(BTD-PZn$_2$)$_n$ chromophores relative to corresponding PZn$_n$ benchmarks

	λ_{max} ($S_0 \rightarrow S_1$)[a] [nm]	$\varepsilon_g@\lambda_{max}$ ($S_0 \rightarrow S_1$) [M^{-1} cm^{-1}]	λ_{max} ($S_1 \rightarrow S_0$) [nm]	FWHM ($S_1 \rightarrow S_0$) [cm^{-1}]	Stokes shift[b] (cm^{-1})	ϕ_f[c,d]	τ_F[e] [ns]	k_r[f] [$\times 10^8$ s^{-1}]	k_{nr}[f] [$\times 10^8$ s^{-1}]
PZn-BTD-PZn	689 (1194)	64 600	741	1605	1018	0.25 (0.31)	1.6	1.6	4.7
PZn-(BTD-PZn)$_2$	745 (1178)	132 700	784	977	543	0.22 (0.36)	1.1	2.0	7.1
PZn-(BTD-PZn)$_4$	777 (1558)	184 000	811	846	490	0.16 (0.29)	0.8	2.0	11
BTD-PZn-BTD	674 (672)	84 000	687	727	281	0.13 (0.13)	1.3	1.0	6.7
BTD-PZn$_2$-BTD	765 (1243)	101 600	787	802	365	0.23 (0.30)	1.4	1.6	5.5
BTD-PZn$_3$-BTD	809 (1663)	157 500	846	872	510	0.16 (0.29)	0.8	2.0	11
BTD-PZn$_5$-BTD	847 (1675)	238 300	888	1008	587	0.10 (0.28)	0.6	1.7	15
PZn$_2$-BTD-PZn$_2$	780 (1822)	145 400	822	926	688	0.14 (0.34)	0.6	2.3	14
PZn$_2$-(BTD-PZn$_2$)$_2$	816 (1582)	340 000	857	1154	586	0.12 (0.36)	0.5	2.4	18
PZn$_2$	695 (1082)	51 400	711	810	324	0.14 (0.16)	1.09	1.3	7.9
PZn$_3$	770 (1386)	116 000	806	875	580	0.19 (0.27)	1.13	1.7	7.1
PZn$_5$	842 (1562)	230 000	883	955	551	0.09 (0.11)	0.45	2.0	20

[a] Numbers in parentheses are spectral breadths (full-widths at half-maximum, FWHM) of the respective transitions in units of cm^{-1}. [b] Stokes shifts values correspond to the difference in energy between the low energy (Q_x) absorption ($S_0 \rightarrow S_1$) and fluorescence ($S_1 \rightarrow S_0$) band maxima. [c] Fluorescence quantum yields (ϕ_f values) were determined using an integrating sphere-based absolute emission quantum yield measurement system (see ESI). [d] Values in parentheses represent those determined in toluene solvent. [e] These values were determined using $S_0 \rightarrow S_2$ excitation (483 nm). Fluorescence lifetimes were measured *via* time-correlated single-photon-counting using a picosecond fluorescence lifetime measurement system. [f] Excited-state relaxation constants were calculated based on the following equations: $\tau_{S1} = 1/(k_r + k_{nr})$, $\phi_f = k_r \times \tau_{S1}$.

maximum (FWHM), Stokes shifts, fluorescence lifetimes (τ_F), radiative rate constant (k_r), non-radiative rate constant (k_{nr}), and fluorescence quantum yield (ϕ_f) data, are tabulated in Table 1 for the **PZn$_n$**, **PZn-(BTD-PZn)$_n$**, **PZn$_2$-(BTD-PZn$_2$)$_n$**, and **BTD-PZn$_n$-BTD** supermolecules.

These fluorescence quantum yield data correspond to absolute measurements, acquired using a calibrated integrating-sphere-based measurement system, which collects photons emitted from the sample following excitation through NIR wavelengths that range up to 1100 nm (see ESI† for a complete system description). Note in this regard that minor differences between the Table 1 ϕ_f data acquired for **PZn$_n$** chromophores and those reported originally[41] stem from the fact that these earlier ϕ_f values were determined *via* the reference method. Table 2 displays comparative integrated oscillator strengths of the B- and Q-band spectral regions of **BTD-PZn$_n$-BTD**, **PZn-(BTD-PZn)$_n$**, and **PZn$_2$-(BTD-PZn$_2$)$_n$** chromophores relative to corresponding **PZn$_n$** benchmarks.

Table 2 Comparative integrated oscillator strengths of the B- and Q-band spectral regions of BTD-PZn$_n$-BTD, PZn-(BTD-PZn)$_n$, and PZn$_2$-(BTD-PZn$_2$)$_n$ chromophores relative to corresponding PZn$_n$ benchmarks[a]

	Oscillator strength B-band region[b]	Oscillator strength Q-band region[c]	Total oscillator strength
PZn-BTD-PZn	2.11	0.72	3.52
PZn-(BTD-PZn)$_2$	4.65	1.03	5.67
PZn-(BTD-PZn)$_4$	5.98	1.58	7.57
BTD-PZn-BTD	2.24	0.37	2.63
BTD-PZn$_2$-BTD	3.54	0.89	4.42
BTD-PZn$_3$-BTD	5.23	1.53	6.76
BTD-PZn$_5$-BTD	7.64	2.10	9.74
PZn$_2$-BTD-PZn$_2$	6.04	1.30	7.35
PZn$_2$-(BTD-PZn$_2$)$_2$	10.49	2.84	13.32
PZn$_2$[d]	2.134	0.303	2.438
PZn$_3$[d]	3.240	0.716	3.956
PZn$_5$[d]	5.986	1.622	7.608

[a] Integrated oscillator strengths (f) were calculated based on the following expression: $f = 4.3 \times 10^{-9} \int \varepsilon dV$, where ε is the experimental extinction coefficient, and ν is the energy (in wave numbers) of the absorption. Values noted derive from electronic absorption spectra recorded in THF solvent. [b] Oscillator strengths calculated over the following wavelength domains: **PZn-BTD-PZn** (~360 to 600 nm); **PZn-(BTD-PZn)$_2$** (~360 to 600 nm); **PZn-(BTD-PZn)$_4$** (~360 to 605 nm); **BTD-PZn-BTD** (~360 to 560 nm); **BTD-PZn$_2$-BTD** (~360 to 560 nm); **BTD-PZn$_3$-BTD** (~360 to 560 nm); **BTD-PZn$_5$-BTD** (~360 to 560 nm); **PZn$_2$-BTD-PZn$_2$** (~360 to 610 nm); **PZn$_2$-(BTD-PZn$_2$)$_2$** (~360 to 610 nm). [c] Oscillator strengths calculated over the following wavelength domains: **PZn-BTD-PZn** (~600 to 760 nm); **PZn-(BTD-PZn)$_2$** (~600 to 820 nm); **PZn-(BTD-PZn)$_4$** (~600 to 900 nm); **BTD-PZn-BTD** (~560 to 720 nm); **BTD-PZn$_2$-BTD** (~560 to 850 nm); **BTD-PZn$_3$-BTD** (~560 to 910 nm); **BTD-PZn$_5$-BTD** (~560 to 1050 nm); **PZn$_2$-BTD-PZn$_2$** (~610 to 860 nm); **PZn$_2$-(BTD-PZn$_2$)$_2$** (~610 to 920 nm). [d] Ref. 41.

Open Access Article. Published on 05 Eost 2020. Downloaded on 2026-05-14 15:42:09.
This article is licensed under a Creative Commons Attribution-NonCommercial 3.0 Unported Licence.

Table 1 highlights that **E-BTD** units that terminate $\mathbf{PZn}_n$ chromophores (Fig. 1A) give rise to **BTD-PZn$_n$-BTD** supermolecules (Fig. 1D) in which $\lambda_{max}(S_1 \rightarrow S_0)$ for **BTD-PZn$_2$-BTD**, **BTD-PZn$_3$-BTD**, and **BTD-PZn$_5$-BTD** redshift by 1358, 587, and 64 cm^{-1}, respectively, relative to their $\mathbf{PZn}_2$, $\mathbf{PZn}_3$, and $\mathbf{PZn}_5$ benchmarks. Note that as a function of the number of PZn units in these arrays, **BTD-PZn$_n$-BTD** and $\mathbf{PZn}_n$ supermolecules display similarly narrow fluorescence FWHM values as well as modest Stokes shifts; these energy differences between the low energy (Q_x) absorption ($S_0 \rightarrow S_1$) and fluorescence ($S_1 \rightarrow S_0$) band maxima of these chromophores range from 325–585 cm^{-1}. A key spectroscopic ramification of terminal ethynyl-BTD conjugation to these $\mathbf{PZn}_n$ frameworks is highlighted in the data chronicled in Table 2, which contrasts the integrated oscillator strengths of the B- and Q-band regions of the electronic absorption spectra of these chromophores. Note that the integrated Q-state oscillator strengths of these **BTD-PZn$_n$-BTD** chromophores are augmented by more than 50% relative their corresponding $\mathbf{PZn}_n$ benchmark. These factors, coupled with a diminished nonradiative rate constant, play important roles in driving the substantial, long-wavelength emission quantum yield manifest by **BTD-PZn$_5$-BTD** ($\phi_f = 0.28$) relative to that for the parent $\mathbf{PZn}_5$ chromophore ($\phi_f = 0.11$) in low dielectric toluene solvent (Table 1).

PZn-(BTD-PZn)$_n$ chromophores (Fig. 1B) contrast the electronic spectral properties of **BTD-PZn$_n$-BTD** supermolecules; **PZn-BTD-PZn**, **PZn-(BTD-PZn)$_2$**, and **PZn-(BTD-PZn)$_4$** display Q_x state absorption maxima that are blue-shifted 126, 436, and 994 cm^{-1} with respect to the $\lambda_{max}(S_0 \rightarrow S_1)$ transitions of their respective $\mathbf{PZn}_2$, $\mathbf{PZn}_3$, and $\mathbf{PZn}_5$ benchmarks (Table 1, Fig. 1); this effect derives from the fact that 4,7-diethynylbenzo[*c*][1,2,5] thiadiazole provides diminished PZn–PZn electronic coupling relative to the ethynyl linker. While **PZn-BTD-PZn** displays an augmented Stokes shift (1018 cm^{-1}) relative to $\mathbf{PZn}_2$ (324 cm^{-1}) due to the greater cumulenic character in its relaxed electronically excited S_1 state,[62] the Stokes shifts manifest for **PZn-(BTD-PZn)$_2$**, **PZn-(BTD-PZn)$_4$**, $\mathbf{PZn}_3$, and $\mathbf{PZn}_5$ are similar in magnitude (~560 cm^{-1}), congruent with more modest structural differences between the relaxed S_0 and S_1 states for these supermolecules (*vide infra*).

PZn-BTD-PZn, **PZn-(BTD-PZn)$_2$**, and **PZn-(BTD-PZn)$_4$** display fluorescence emission maxima centered at 741, 784, and 811 nm, respectively, and substantial fluorescence quantum yields in THF solvent [ϕ_f(**PZn-BTD-PZn**) = 0.25; ϕ_f(**PZn-(BTD-PZn)$_2$**) = 0.22; ϕ_f(**PZn-(BTD-PZn)$_4$**) = 0.16]. Similar to that observed for **BTD-PZn$_n$-BTD** chromophores, fluorescence quantum yields are significantly enhanced in nonpolar solvent; note in this regard that ϕ_f(**PZn-(BTD-PZn)$_4$**) is amplified to 29% in toluene (Table 1).

Fig. 1C highlights the absorptive and emissive spectral properties that ensue when $\mathbf{PZn}_2$ chromophores are linked by 4,7-diethynylbenzo[*c*][1,2,5]thiadiazole units. These **PZn$_2$-(BTD-PZn$_2$)$_n$** chromophores display dramatic Q_x absorption band intensification with increasing conjugation (Tables 1 and 2); note in this regard that **PZn$_2$-(BTD-PZn$_2$)$_n$** is an exceptional long-wavelength absorber (ε(816 nm) = 340 000 M^{-1} cm^{-1}; Table 1). **PZn$_2$-BTD-PZn$_2$** and **PZn$_2$-(BTD-PZn$_2$)$_2$** emit respectively at 822 and 857 nm in THF solvent, with corresponding quantum yields of 14 and 12%. As demonstrated for both **PZn-(BTD-PZn)$_n$** and **BTD-PZn$_n$-BTD** chromophores, these fluorescence quantum yields are dramatically enhanced in toluene solvent [ϕ_f(**PZn$_2$-BTD-PZn$_2$**) = 0.34; ϕ_f(**PZn$_2$-(BTD-PZn$_2$)$_2$**) = 0.36]. These data acquired for **PZn$_2$-(BTD-PZn$_2$)$_n$** designs suggest additional approaches to realize related frameworks that make possible high quantum yield NIR emission that include electronic modulation of the proquinoidal units that both terminate supermolecules that utilize $\mathbf{PZn}_n$ building blocks, as well as those that are integrated into the conjugated backbones of these compositions.

Computed electronic structures of BTD-PZn$_n$-BTD, PZn-(BTD-PZn)$_n$, and PZn$_2$-(BTD-PZn$_2$)$_n$ chromophores

The natures of the low energy S_1 states of **BTD-PZn$_n$-BTD**, **PZn-(BTD-PZn)$_n$**, and **PZn$_2$-(BTD-PZn$_2$)$_n$** chromophores were probed through frontier orbital (FO) population and transition matrix

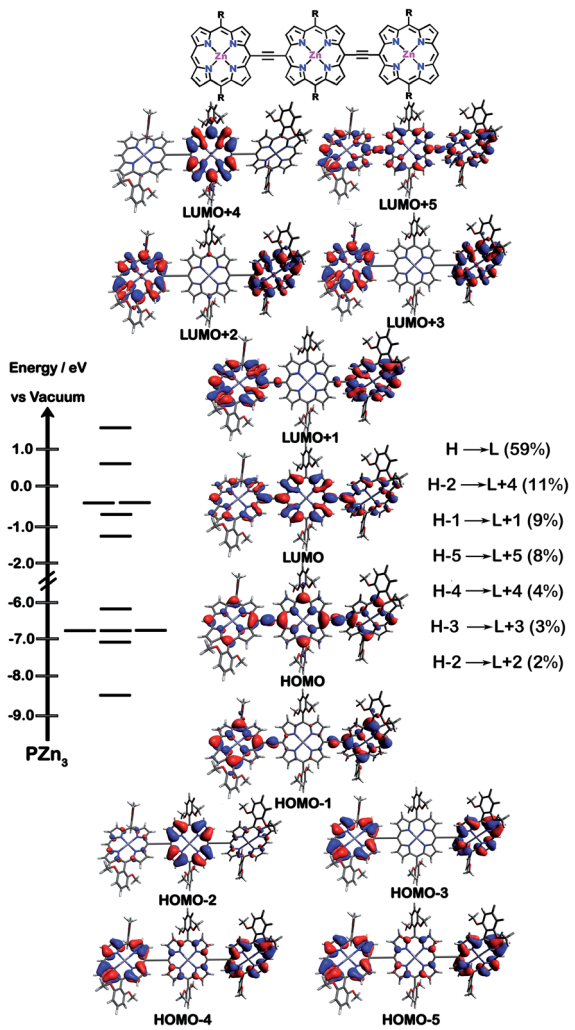

Fig. 2 Calculated frontier molecular orbitals, energy levels, and relative one-electron configurations that contribute to the lowest energy (Q_x) transition for the $\mathbf{PZn}_3$ benchmark. Calculations were performed at the M11/6-311g(d) theory level.

This journal is © The Royal Society of Chemistry 2020

Open Access Article. Published on 05 Eost 2020. Downloaded on 2026-05-14 15:42:09.
This article is licensed under a Creative Commons Attribution-NonCommercial 3.0 Unported Licence.

eigenvector analyses derived using TD-DFT methods. Fig. 2–4 show FO diagrams for **BTD-PZn$_3$-BTD**and **PZn-(BTD-PZn)$_2$**, along with those for the **PZn$_3$** benchmark, and highlight the prominent one-electron configurations that contribute to their respective lowest energy Q_x transitions; related data for the **PZn$_2$-(BTD-PZn$_2$)$_2$** chromophore is presented in the ESI.†

The natures and energy separations between the **PZn$_3$**, **BTD-PZn$_3$-BTD**, and **PZn-(BTD-PZn)$_2$** FOs underscore the x-polarized nature of the lowest energy excited state for these supermolecules, and the globally delocalized character of their respective S_1 excited states. The low-lying excited states of these supermolecules are described by extensive configuration interaction (CI). The $S_0 \rightarrow S_1$ transitions of **PZn$_3$**, **BTD-PZn$_3$-BTD**, and **PZn-(BTD-PZn)$_2$** have large contributions (~55%) from the one electron HOMO → LUMO (H → L) configuration, and highlight the importance of quinoidal resonance contributions to this low-lying excited state; this resonance contribution plays a key role in the solvent-dielectric dependent fluorescence quantum yields evidenced in THF and toluene solvent.

For **PZn$_3$** (Fig. 2), seven single excitation configurations describe the transition matrix eigenvector; in contrast, nine and six single excitation configurations describe respectively the transition matrix eigenvectors for **BTD-PZn$_3$-BTD** and **PZn-(BTD-PZn)$_2$**. For **PZn$_3$**, the transition eigenvector is dominated by configurations (representing an ~82% weighting in the CI expansion) that do not redistribute to a significant degree electron density. For **BTD-PZn$_3$-BTD** and **PZn-(BTD-PZn)$_2$**, the relative importance of such single excitation configurations that do not redistribute significantly electron density drops respectively to 74 and 22%, highlighting the increased importance of single-excitation configurations that redistribute electron density in the CI expansions that describe the $S_0 \rightarrow S_1$ transition eigenvectors for these supermolecules. While the bandgap represented by $\Delta E_{\mathrm{HOMO-LUMO}}$ varies to a minor degree and spans ~4.5 to 4.8 eV, note that the FO bandwidth in these Fig. 2–4 fluorophores varies significantly: $\Delta_{\mathrm{H-5-L+5}}$ for **PZn$_3$** is 9.77 eV but only 7.76 eV for **PZn-(BTD-PZn)$_2$**, a decrease of 2.01 eV.

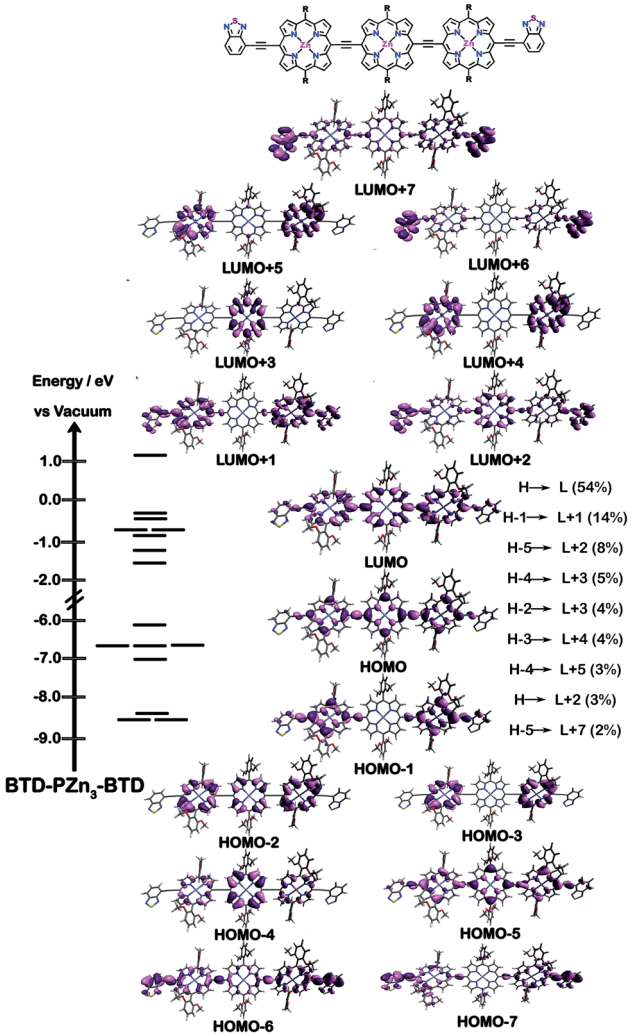

Fig. 3 Calculated frontier molecular orbitals, energy levels, and relative one-electron configurations that contribute to the lowest energy (Q_x) transition for BTD-PZn$_3$-BTD. Calculations were performed at the M11/6-311g(d) theory level.

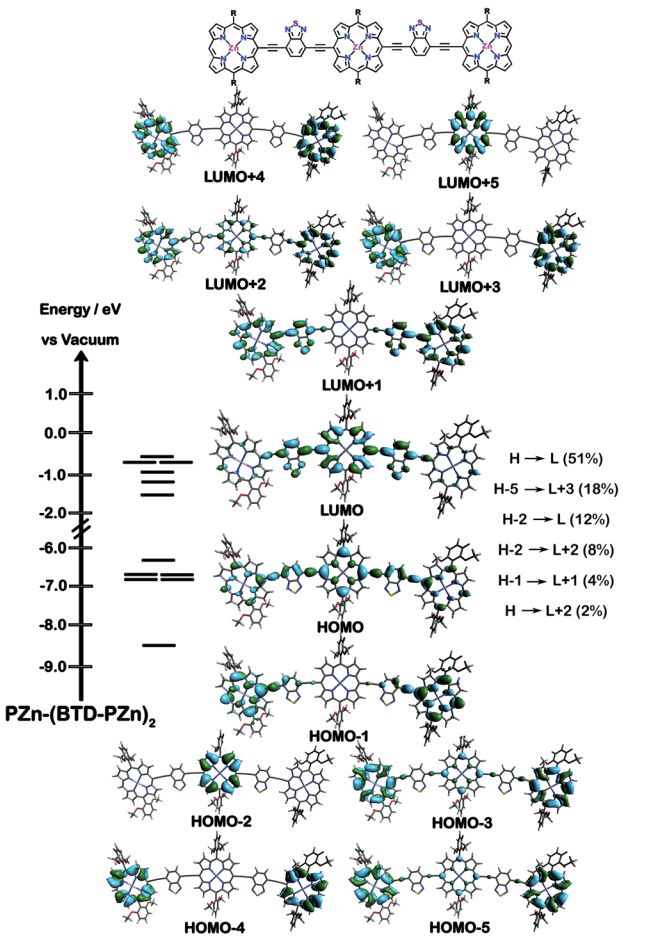

Fig. 4 Calculated frontier molecular orbitals, energy levels, and relative one-electron configurations that contribute to the lowest energy (Q_x) transition for PZn-(BTD-PZn)$_2$. Calculations were performed at the M11/6-311g(d) theory level.

Open Access Article. Published on 05 Eost 2020. Downloaded on 2026-05-14 15:42:09.
This article is licensed under a Creative Commons Attribution-NonCommercial 3.0 Unported Licence.

Note that as supermolecular conjugation evolves from **PZn$_3$** to **BTD-PZn$_3$-BTD** and **PZn-(BTD-PZn)$_2$**, an increased degeneracy of energy eigenvalues is manifest in the Fig. 2–4 FOs. This increased density of states (DOS) evident in **BTD-PZn$_3$-BTD** and **PZn-(BTD-PZn)$_2$** derives from the mixing of BTD and PZn frontier orbitals. Congruent with Fermi's Golden Rule, transition probability correlates with increased DOS. This larger DOS near the HOMO and LUMO levels serve to increase the multireference nature of the S_1 state wave function; S_1 configurations that involve these delocalized and mixed frontier orbitals will thus exhibit enhanced S_1 state wave function spatial delocalization. This computational trend is in line with the experimentally determined transition moments, wherein Q_x-transition oscillator strengths for **BTD-PZn$_3$-BTD** and **PZn-(BTD-PZn)$_2$** exceed that of **PZn$_3$**. Note also that this dispersion of FO energies, which decreases progressively from **PZn$_3$** to **BTD-PZn$_3$-BTD** to **PZn-(BTD-PZn)$_2$** (Fig. 2–4), is correlated with increased π conjugation which is reflected in the computed electronic delocalization range function for these fluorophores (ESI†); due to the nature of these orbitals and their diminished energy gaps within the filled and empty regimes of the FO manifold, a greater weighted fraction of single excitation configurations having charge resonance character is manifest, congruent with the augmented Q_x absorption oscillator strengths observed for **BTD-PZn$_n$-BTD** and **PZn-(BTD-PZn)$_n$** relative to **PZn$_n$** (Fig. 1, Tables 1 and 2).

Conclusions

We describe a design strategy for (porphinato)zinc-based supermolecules that possess large NIR fluorescence quantum yields. These **PZn-(BTD-PZn)$_n$**, **PZn$_2$-(BTD-PZn$_2$)$_n$**, and **BTD-PZn$_n$-BTD** fluorophores feature either 4-ethynylbenzo[*c*][1,2,5]thiadiazole (**E-BTD**) units that terminate *meso*-to-*meso* ethyne-bridged (porphinato)zinc (**PZn$_n$**) arrays, or 4,7-diethynylbenzo[*c*][1,2,5]thiadiazole (**E-BTD-E**) spacers that are integrated into the backbone of these compositions. **PZn-(BTD-PZn)$_n$**, **PZn$_2$-(BTD-PZn$_2$)$_n$**, and **BTD-PZn$_n$-BTD** chromophores are characterized by enhanced transfer of B-to-x-polarized Q-state oscillator strength relative to their corresponding **PZn$_n$** benchmarks, intensified Q_x absorption bands, supermolecule structural rigidification, spectrally narrow fluorescence emission bands, small magnitude Stokes shifts, and large radiative rate constant magnitudes. TD-DFT calculations point to the importance of a greater weighted fraction of single excitation configurations having charge resonance character that describe the $S_0 \rightarrow S_1$ transition matrix eigenvector in **PZn-(BTD-PZn)$_n$**, **PZn$_2$-(BTD-PZn$_2$)$_n$**, and **BTD-PZn$_n$-BTD** emitters relative to **PZn$_n$** oscillators in driving these spectroscopic and dynamical properties. Collectively, these systems define an unusual family of intensely absorbing vis-NIR absorbers that display strikingly high fluorescence quantum yields (ϕ_f values) over the 700–900 nm regime of the NIR. These THF ϕ_f values for **PZn-(BTD-PZn)$_n$**, **PZn$_2$-(BTD-PZn$_2$)$_n$**, and **BTD-PZn$_n$-BTD** supermolecules, perhaps without peer in a solvent of this dielectric strength over this spectral window, range from 10–25%; notably these ϕ_f values are dramatically amplified in hydrophobic media and thus contrast the behavior of classic tricarbocyanine NIR dyes, displaying fluorescence quantum yields ranging from 28–36% in toluene solvent. Because these **BTD-PZn$_n$-BTD**, **PZn-(BTD-PZn)$_n$**, and **PZn$_2$-(BTD-PZn$_2$)$_n$** supermolecules display extraordinarily large NIR fluorescence quantum yields in hydrophobic solvent, these designs underscore new opportunities to evolve NIR-emissive nano- and mesoscale vesicles for fluorescence imaging applications in which the emissive irradiance exceeds the impressive metrics already established for such structures that membrane-disperse **PZn$_n$** fluorophores.[54–61,65]

Experimental section

Synthesis and characterization

The synthetic procedures and corresponding characterization data of all new compounds, complete with the reaction schemes, are given in the ESI.†

Instrumentation

Electronic absorption spectra were recorded on a Shimadzu UV-1700 spectrophotometer. Steady-state emission spectra were recorded on a FLS920 spectrometer that utilized a xenon lamp (Xe900) as the excitation light source and an extended red sensitive PMT (Hamamatsu R2658P side window photomultiplier, spectral range: 200–1010 nm) for detection. Emission spectra were corrected using a calibration curve supplied with the instrument.

Fluorescence lifetime measurements

Time-resolved emission spectra were recorded using a Hamamatsu C4780 picosecond fluorescence lifetime measurement system. This system employs a Hamamatsu Streakscope C4334 as its photon-counting detector; a Hamamatsu C4792-01 synchronous delay generator electronically generated all time delays. The excitation light source chosen was a Hamamatsu 405 nm diode laser. Fluorescence lifetimes were acquired in single-photon-counting mode using Hamamatsu HPD-TA software and analyzed using the Hamamatsu fitting module.

Quantum yield measurements

A Hamamatsu C9920-03 Absolute Quantum Yield Measurement System was employed to make the quantum yield measurements. Excitation initiates from a Xe-lamp, where the wavelength is selected by a monochromator, and passed through a 1 mm optical excitation fiber. The inside of the sphere is coated with Spectralon (Labsphere, Inc.) that has at least 99% reflectance over the 350–1650 nm spectral window. Added detail regarding these measurements is provided in the ESI.†

Time-dependent density functional theory calculations

All electronic structure calculations were performed upon model compounds in which aliphatic chains were truncated to methyl groups (ESI†). Structure optimization and linear response calculations were performed with density functional theory (DFT) using Gaussian 16, revision C.01.[67] The M11 [68]

 This journal is © The Royal Society of Chemistry 2020

Open Access Article. Published on 05 Eost 2020. Downloaded on 2026-05-14 15:42:09.
This article is licensed under a Creative Commons Attribution-NonCommercial 3.0 Unported Licence.

functional was employed for all calculations. Optimizations were performed with minimal symmetry constraints using tight optimization criteria with the 6-311g(d) basis set implemented. Selected frontier orbital wave functions were plotted as isosurfaces (iso = 0.02) using Avogadro.[69] TD-DFT result files were post-processed using the GaussSum package;[70] this software partitions the wave function amplitudes onto atomic components using Mulliken population analysis,[71] and parses the electronic configurations contributing to each excitation.

Conflicts of interest

No competing financial interests have been declared.

Acknowledgements

This work was funded by the Division of Chemical Sciences, Geosciences, and Biosciences, Office of Basic Energy Sciences, of the U.S. Department of Energy through Grant DE-SC0001517. The authors are grateful for support made available through the Extreme Science and Engineering Discovery Environment (XSEDE) Comet at the San Diego Supercomputer Center through allocation CHE190106, which is supported by the National Science Foundation through Grant ACI-1548562. E. J. P. acknowledges the National Science Foundation for a Graduate Research Fellowship.

References

1 A. Ajayaghosh, *Chem. Soc. Rev.*, 2003, **32**, 181–191.
2 L.-Y. Lin, Y.-H. Chen, Z.-Y. Huang, H.-W. Lin, S.-H. Chou, F. Lin, C.-W. Chen, Y.-H. Liu and K.-T. Wong, *J. Am. Chem. Soc.*, 2011, **133**, 15822–15825.
3 Z. Li, T.-H. Park, J. Rawson, M. J. Therien and E. Borguet, *Nano Lett.*, 2012, **12**, 2722–2727.
4 G. Li, R. Zhu and Y. Yang, *Nat. Photonics*, 2012, **6**, 153–161.
5 Y. F. Deng, J. Liu, J. T. Wang, L. H. Liu, W. L. Li, H. K. Tian, X. J. Zhang, Z. Y. Xie, Y. H. Geng and F. S. Wang, *Adv. Mater.*, 2014, **26**, 471–476.
6 C. Liu, K. Wang, X. Gong and A. J. Heeger, *Chem. Soc. Rev.*, 2016, **45**, 4825–4846.
7 G. Li, W.-H. Chang and Y. Yang, *Nat. Rev. Mater.*, 2017, **2**, 17043.
8 Y.-J. Cheng, S.-H. Yang and C.-S. Hsu, *Chem. Rev.*, 2009, **109**, 5868–5923.
9 Y. Zhao, Y. Guo and Y. Liu, *Adv. Mater.*, 2013, **25**, 5372–5391.
10 C. W. Spangler, *J. Mater. Chem.*, 1999, **9**, 2013–2020.
11 M. Grätzel, *J. Photochem. Photobiol., C*, 2003, **4**, 145–153.
12 A. Hagfeldt, G. Boschloo, L. C. Sun, L. Kloo and H. Pettersson, *Chem. Rev.*, 2010, **110**, 6595–6663.
13 T. N. Singh-Rachford and F. N. Castellano, *Coord. Chem. Rev.*, 2010, **254**, 2560–2573.
14 T. N. Singh-Rachford, A. Nayak, M. L. Muro-Small, S. Goeb, M. J. Therien and F. N. Castellano, *J. Am. Chem. Soc.*, 2010, **132**, 14203–14211.
15 J. Z. Zhao, S. M. Ji and H. M. Guo, *RSC Adv.*, 2011, **1**, 937–950.
16 J. Z. Zhao, W. H. Wu, J. F. Sun and S. Guo, *Chem. Soc. Rev.*, 2013, **42**, 5323–5351.
17 J.-H. Olivier, Y. Bai, H. Uh, H. Yoo, M. J. Therien and F. N. Castellano, *J. Phys. Chem. A*, 2015, **119**, 5642–5649.
18 J. C. Ostrowski, K. Susumu, M. R. Robinson, M. J. Therien and G. C. Bazan, *Adv. Mater.*, 2003, **15**, 1296–1300.
19 A. C. Grimsdale, K. L. Chan, R. E. Martin, P. G. Jokisz and A. B. Holmes, *Chem. Rev.*, 2009, **109**, 897–1091.
20 L. Dou, Y. Liu, Z. Hong, G. Li and Y. Yang, *Chem. Rev.*, 2015, **115**, 12633–12665.
21 D. N. Beratan, J. N. Onuchic and J. W. Perry, *J. Phys. Chem.*, 1987, **91**, 2696–2698.
22 D. N. Beratan, *J. Phys. Chem. Lett.*, 1989, **93**, 3915–3920.
23 T. V. Duncan, K. Song, S.-T. Hung, I. Miloradovic, A. Nayak, A. Persoons, T. Verbiest, M. J. Therien and K. Clays, *Angew. Chem., Int. Ed.*, 2008, **47**, 2978–2981.
24 G. Heimel, *ACS Cent. Sci.*, 2016, **2**, 309–315.
25 J. V. Frangioni, *Curr. Opin. Chem. Biol.*, 2003, **7**, 626–634.
26 M. Y. Berezin and S. Achilefu, *Chem. Rev.*, 2010, **110**, 2641–2684.
27 L. Yuan, W. Lin, K. Zheng, L. He and W. Huang, *Chem. Soc. Rev.*, 2013, **42**, 622–661.
28 S. J. Strickler and R. A. Berg, *J. Chem. Phys.*, 1962, **37**, 814–822.
29 R. Englman and J. Jortner, *Mol. Phys.*, 1970, **18**, 145–164.
30 V. S.-Y. Lin, S. G. DiMagno and M. J. Therien, *Science*, 1994, **264**, 1105–1111.
31 P. J. Angiolillo, V. S.-Y. Lin, J. M. Vanderkooi and M. J. Therien, *J. Am. Chem. Soc.*, 1995, **117**, 12514–12527.
32 V. S.-Y. Lin and M. J. Therien, *Chem.–Eur. J.*, 1995, **1**, 645–651.
33 R. Kumble, S. Palese, V. S.-Y. Lin, M. J. Therien and R. M. Hochstrasser, *J. Am. Chem. Soc.*, 1998, **120**, 11489–11498.
34 R. Shediac, M. H. B. Gray, H. T. Uyeda, R. C. Johnson, J. T. Hupp, P. J. Angiolillo and M. J. Therien, *J. Am. Chem. Soc.*, 2000, **122**, 7017–7033.
35 P. J. Angiolillo, K. Susumu, H. T. Uyeda, V. S.-Y. Lin, R. Shediac and M. J. Therien, *Synth. Met.*, 2001, **116**, 247–253.
36 J. T. Fletcher and M. J. Therien, *Inorg. Chem.*, 2002, **41**, 331–341.
37 K. Susumu and M. J. Therien, *J. Am. Chem. Soc.*, 2002, **124**, 8550–8552.
38 I. V. Rubtsov, K. Susumu, G. I. Rubtsov and M. J. Therien, *J. Am. Chem. Soc.*, 2003, **125**, 2687–2696.
39 P. J. Angiolillo, H. T. Uyeda, T. V. Duncan and M. J. Therien, *J. Phys. Chem. B*, 2004, **108**, 11893–11903.
40 K. Susumu, P. R. Frail, P. J. Angiolillo and M. J. Therien, *J. Am. Chem. Soc.*, 2006, **128**, 8380–8381.
41 T. V. Duncan, K. Susumu, L. E. Sinks and M. J. Therien, *J. Am. Chem. Soc.*, 2006, **128**, 9000–9001.
42 P. R. Frail, K. Susumu, M. Huynh, J. Fong, J. M. Kikkawa and M. J. Therien, *Chem. Mater.*, 2007, **19**, 6062–6064.
43 T. V. Duncan, T. Ishizuka and M. J. Therien, *J. Am. Chem. Soc.*, 2007, **129**, 9691–9703.

Open Access Article. Published on 05 Eost 2020. Downloaded on 2026-05-14 15:42:09.
This article is licensed under a Creative Commons Attribution-NonCommercial 3.0 Unported Licence.

44 T. V. Duncan, P. R. Frail, I. R. Miloradovic and M. J. Therien, *J. Phys. Chem. B*, 2010, **114**, 14696–14702.
45 J. Rawson, P. J. Angiolillo and M. J. Therien, *Proc. Natl. Acad. Sci. U. S. A.*, 2015, **112**, 13779–13783.
46 Y. Bai, J.-H. Olivier, H. Yoo, N. F. Polizzi, J. Park, J. Rawson and M. J. Therien, *J. Am. Chem. Soc.*, 2017, **139**, 16946–16958.
47 R. R. Birge and F. J. Duarte, *Kodak Optical Products*, Kodak Publication, Rochester, New York, 1990, Publication JJ-169B.
48 J. Gayton, S. A. Autry, W. Meador, S. R. Parkin, G. A. Hill Jr, N. I. Hammer and J. H. Delcamp, *J. Org. Chem.*, 2019, **84**, 687–697.
49 W. E. Meador, S. A. Autry, R. N. Bessetti, J. N. Gayton, A. S. Flynt, N. I. Hammer and J. H. Delcamp, *J. Org. Chem.*, 2020, **85**, 4089–4095.
50 S. Reindl, A. Penzkofer, S.-H. Gong, M. Landthaler, R. M. Szeimies, C. Abels and W. Bäumler, *J. Photochem. Photobiol., A*, 1997, **105**, 65–68.
51 Y. Lin, R. Weissleder and C.-H. Tung, *Bioconjugate Chem.*, 2002, **13**, 605–610.
52 P. J. Angiolillo, J. Rawson, P. R. Frail and M. J. Therien, *Chem. Commun.*, 2013, **49**, 9722–9724.
53 S. Richert, G. Bullard, J. Rawson, P. J. Angiolillo, M. J. Therien and C. R. Timmel, *J. Am. Chem. Soc.*, 2017, **139**, 5301–5304.
54 P. P. Ghoroghchian, P. R. Frail, K. Susumu, D. Blessington, A. K. Brannan, F. S. Bates, B. Chance, D. A. Hammer and M. J. Therien, *Proc. Natl. Acad. Sci. U. S. A.*, 2005, **102**, 2922–2927.
55 P. P. Ghoroghchian, P. R. Frail, K. Susumu, T.-H. Park, S. P. Wu, H. T. Uyeda, D. A. Hammer and M. J. Therien, *J. Am. Chem. Soc.*, 2005, **127**, 15388–15390.
56 N. A. Christian, M. C. Milone, S. S. Ranka, G. Li, P. R. Frail, K. P. Davis, F. S. Bates, M. J. Therien, P. P. Ghoroghchian, C. H. June and D. A. Hammer, *Bioconjugate Chem.*, 2007, **18**, 31–40.
57 P. P. Ghoroghchian, P. R. Frail, G. Li, J. A. Zupancich, F. S. Bates, D. A. Hammer and M. J. Therien, *Chem. Mater.*, 2007, **19**, 1309–1318.
58 N. A. Christian, F. Benencia, M. C. Milone, G. Li, P. R. Frail, M. J. Therien, G. Coukos and D. A. Hammer, *Mol. Imaging Biol.*, 2009, **11**, 167–177.
59 G. P. Robbins, R. L. Saunders, J. B. Haun, J. Rawson, M. J. Therien and D. A. Hammer, *Langmuir*, 2010, **26**, 14089–14096.
60 N. P. Kamat, Z. Liao, L. E. Moses, J. Rawson, M. J. Therien, I. J. Dmochowski and D. A. Hammer, *Proc. Natl. Acad. Sci. U. S. A.*, 2011, **108**, 13984–13989.
61 C. L. Hofmann, M. C. O'Sullivan, A. Detappe, Y. Yu, X. Yang, W. Qi, C. D. Landon, M. J. Therien, M. W. Dewhirst, P. P. Ghoroghchian and G. M. Palmer, *Nanoscale*, 2017, **9**, 13465–13476.
62 K. Susumu, T. V. Duncan and M. J. Therien, *J. Am. Chem. Soc.*, 2005, **127**, 5186–5195.
63 Y. Bai, J. Rawson, S. A. Roget, J.-H. Olivier, J. Lin, P. Zhang, D. N. Beratan and M. J. Therien, *Chem. Sci.*, 2017, **8**, 5889–5901.
64 H. T. Uyeda, Y. Zhao, K. Wostyn, I. Asselberghs, K. Clays, A. Persoons and M. J. Therien, *J. Am. Chem. Soc.*, 2002, **124**, 13806–13813.
65 T. V. Duncan, P. P. Ghoroghchian, I. V. Rubtsov, D. A. Hammer and M. J. Therien, *J. Am. Chem. Soc.*, 2008, **130**, 9773–9784.
66 K. Susumu and M. J. Therien, *J. Porphyrins Phthalocyanines*, 2015, **19**, 205–218.
67 M. J. Frisch, G. W. Trucks, H. B. Schlegel, G. E. Scuseria, M. A. Robb, J. R. Cheeseman, G. Scalmani, V. Barone, G. A. Petersson, H. Nakatsuji, X. Li, M. Caricato, A. V. Marenich, J. Bloino, B. G. Janesko, R. Gomperts, B. Mennucci, H. P. Hratchian, J. V. Ortiz, A. F. Izmaylov, J. L. Sonnenberg, D. Williams-Young, F. Ding, F. Lipparini, F. Egidi, J. Goings, B. Peng, A. Petrone, T. Henderson, D. Ranasinghe, V. G. Zakrzewski, J. Gao, N. Rega, G. Zheng, W. Liang, M. Hada, M. Ehara, K. Toyota, R. Fukuda, J. Hasegawa, M. Ishida, T. Nakajima, Y. Honda, O. Kitao, H. Nakai, T. Vreven, K. Throssell, J. A. Montgomery Jr, J. E. Peralta, F. Ogliaro, M. J. Bearpark, J. J. Heyd, E. N. Brothers, K. N. Kudin, V. N. Staroverov, T. A. Keith, R. Kobayashi, J. Normand, K. Raghavachari, A. P. Rendell, J. C. Burant, S. S. Iyengar, J. Tomasi, M. Cossi, J. M. Millam, M. Klene, C. Adamo, R. Cammi, J. W. Ochterski, R. L. Martin, K. Morokuma, O. Farkas, J. B. Foresman and D. J. Fox, *Gaussian 16, Revision C.01*, 2016.
68 R. Peverati and D. G. Truhlar, *J. Phys. Chem. Lett.*, 2011, **2**, 2810–2817.
69 M. D. Hanwell, D. E. Curtis, D. C. Lonie, T. Vandermeersch, E. Zurek and G. R. Hutchison, *J. Cheminf.*, 2012, **4**, 17.
70 N. M. O'Boyle, A. L. Tenderholt and K. M. Langner, *J. Comput. Chem.*, 2008, **29**, 839–845.
71 R. S. Mulliken, *J. Chem. Phys.*, 1955, **23**, 1833–1840.

This journal is © The Royal Society of Chemistry 2020